WIRELESS COMMUNICATIONS AND MOBILE COMPUTING
Wirel. Commun. Mob. Comput. 2016; **16**:3408–3422
Published online 20 January 2017 in Wiley Online Library (wileyonlinelibrary.com). DOI: 10.1002/wcm.2766

RESEARCH ARTICLE

Efficient handover measurement technique for small-cell networks using a virtual cell synchronization signal

Rothna Pec[1], Chang Hwan Park[2] and Yong Soo Cho[1]*

[1] School of Electrical and Electronics Engineering, Chung-Ang University, Seoul, Korea
[2] Advanced Communication Technology Laboratory, LG Electronics, Seoul, Korea

ABSTRACT

A small-cell network (SCN) constructed by splitting a macro-cell into numerous small cells using an active antenna array system is studied. A synchronization signal appropriate for the SCN, virtually generated by an eNodeB with 3D beamforming, is proposed for efficient handover in SCNs. The virtual cell synchronization signal (VCSS) carries a macro-cell ID (MCID) and virtual-cell ID (VCID) in a hierarchical manner, allowing us to distinguish between an intra-cell handover (virtual cell handover within a cell without changing the serving eNodeB) and inter-cell handover (virtual cell handovers across cells while changing the serving eNodeB) in SCNs. Using the signal metrics obtained by the VCSS, an efficient handover measurement technique is proposed which can significantly reduce the processing time and overhead by distinguishing between the intra-cell/inter-cell handovers. The performance of the proposed technique is evaluated by simulating two different deployment scenarios of LTE-based SCN with 3D beamforming.

KEYWORDS

small cell network; virtual cell synchronization signal; 3D beamforming; handover; inter-cell handover; intra-cell handover

***Correspondence**

Yong Soo Cho, School of Electrical and Electronics Engineering, Chung-Ang University, Seoul, Korea.
E-mail: yscho@cau.ac.kr

1. INTRODUCTION

Owing to the explosive increase in mobile data traffic, different approaches have been investigated for future broadband cellular communication systems. The millimeter-wave frequency spectrum, massive multiple-input multiple-output systems, and small-cell networks (SCNs) are expected to be possible candidates that can boost system capacity to meet new requirements [1]. An SCN achieves network densification by reducing the cell size and increasing the spatial reuse of the spectrum, and its capability to improve the network capacity is much greater than those provided by increasing the spectrum and spectral efficiency combined [2]. Network densification, configured by dynamically deploying a large number of small and low-power eNodeB, has attracted attention from research engineers in both academia and industry because it can effectively increase network capacity by a factor of 40 compared to traditional deployment [3,4]. One way to build an SCN is to split each macro-cell into numerous small cells using an active antenna array system (AAS) at the eNodeB.

Unlike a passive AAS, where each antenna element cannot be electronically controlled, an AAS can provide dynamic beam control in both the azimuth and elevation domains by electronically changing the weight value of each antenna. Full-dimensional sectorization (full-dimensional spatial division multiple access) can be achieved using a 3D beamforming technique at an eNodeB equipped with an AAS [5,6]. For example, user equipments (UEs) on different floors of a building, in a hot spot or any specific region, can be separately served by individual 3D beams with full bandwidth [6–8]. In this paper, each small cell generated by 3D beamforming is referred to as a virtual cell, in the sense that each small cell is virtually generated by an eNodeB with 3D beamforming rather than by the separate deployment of an actual low-power eNodeB. We consider two different deployment scenarios: terrestrial deployment and balloon-based deployment. For terrestrial deployment, an AAS is

installed at each eNodeB; whereas, for balloon-based deployment, AASs are attached to individual balloons in the sky at appropriate altitudes.

A network of virtual cells within the vicinity of an eNodeB can be regarded as a synchronous network because virtual cells are generated simultaneously by each eNodeB with a set of 3D beams. Thus, there will be no significant synchronization issues for frequency, time, and phase in a virtual-cell network, unlike an actual-deployment-based SCN [9]. However, an efficient handover technique needs to be developed for any type of SCN because frequent handovers normally occur in SCNs owing to their small cell size. So far, most of the handover algorithms developed for SCNs have been based on the traditional handover technique used in macrocells [10], which is not adequate for SCNs that are virtually generated by 3D beamforming. In addition, PCI confusion problem needs to be resolved as the number of IDs to be supported in SCNs can be significantly increased.

In this paper, we propose a virtual cell synchronization signal (VCSS) that allows for an efficient handover in a virtual-cell network constructed using eNodeBs with 3D beamforming. The VCSS satisfies both the constant-amplitude zero-autocorrelation (CAZAC) property and the subset orthogonality property. In the proposed approach, synchronization signals are designed in a hierarchical manner. That is, the same macro-cell ID (MCID) is assigned to virtual cells in the same cell, and a different virtual-cell ID (VCID) is assigned to each virtual cell in the cell to differentiate between virtual cells. The VCIDs are reused in adjacent cells because their MCIDs are normally different, allowing us to generate a large set of sequences. The MCID is carried by the PSS and SSS as in the LTE system, while the VCID is carried by the VCSS. Because the VCID needs to be detected in a multi-cell environment, the VCSS is designed in such a way that the VCID is mapped to the sequence in conjunction with its MCID. By designing the VCSS in a hierarchical manner, the number of IDs to be supported in an SCN can be significantly increased, overcoming the PCI confusion problem. In addition, the VCSS allows us to distinguish between an intra-cell handover and an inter-cell handover in a virtual-cell network [11]. Based on measurements of signal strengths from the received VCSS, we propose an efficient handover technique that can significantly reduce the processing time and overhead by distinguishing between intra-cell and inter-cell handovers.

The rest of this paper is organized as follows. Section II summarizes handover techniques developed for SCNs (cellular networks with femtocells). Section III describes a VCSS appropriate for SCNs (virtually generated by an eNodeB with 3D beamforming) and discusses the properties of the VCSS. An efficient handover measurement technique using the VCSS is proposed for SCNs in Section IV. In Section V, the performance of the proposed technique is evaluated by simulation for LTE-based SCNs with 3D beamforming. Finally, conclusions are drawn in Section VI.

2. RELATED WORKS

In this section, we summarize handover techniques developed for two-tier networks (macrocell and femtocell). In [12], a handover algorithm based on the received signal strengths (RSSs) reported by a nonsubscriber was proposed for orthogonal frequency division multiple access (OFDMA) two-tier macrocell–femtocell networks by providing the priority to the intra-cell handover for interference and handover mitigation. The main idea of this paper is that when a nonsubscriber connected to a macrocell suffers from cross-tier interference because of a nearby femtocell, the macrocell itself performs an intra-cell handover if possible. The priority is given to intra-cell handover by changing the used sub-channel to the other available sub-channel of the serving macro-cell with less interference.

In [13], a handover decision algorithm based on the RSS of femtocell and location prediction of UE was proposed to reduce the unnecessary handover in macrocell–femtocell networks. In this approach, next sub-area movement patterns are predicted through the movement pattern analysis when a UE approaches the femtocell. The main idea is to keep macrocell connection rather than conducting macrocell-to-femtocell handover when the UE may be a temporary femtocell visitor (who stays in the femtocell for a relatively short time). In [14,15], handover algorithms based on the awareness of UE's speed in addition to RSS were proposed for cellular network with femtocells. The authors proposed handover algorithms based on the mobility state because UEs with high velocities moving through femtocells usually lead to performing unnecessary handovers. Here, the UEs in free mode (where UE's mobility is lower than the predefined threshold value) is allowed to make handover to the femtocell. In [16], a handover decision policy based on the legacy LTE handover technique was proposed to reduce the power consumption at the UE and to lower the interferences in two-tier networks. The proposed policy is LTE backward-compatible because it can be easily employed by adapting the handover hysteresis margin with respect to a prescribed SINR target and standard LTE measurements.

The handover algorithms discussed in [12–15], and [16] do not take into account the power discrepancy between macro eNodeB and femto eNodeB. However, the conventional handover algorithm based on the RSS with hysteresis and threshold cannot be applied to macrocell–femtocell networks directly because there is a large difference in the transmit power of macro eNodeB and femto eNodeB. In [17] and [18], efficient handover algorithms were developed for macrocell–femtocell networks considering the discrepancy in transmit power between macro eNodeB and femto eNodeB. In [17], a new RSS-based handover algorithm was proposed by combining the RSSs from both a serving macro eNodeB and a target femto eNodeB. Also, a method of determining an optimal value was proposed for the

combination factor that reflects large asymmetry in the transmit power of the cells. In [18], a new handover algorithm which makes both the RSS and wireless transmission loss between UE to macrocell and UE to femtocell was proposed. It was shown that the handover algorithm can improve the utilization of femtocells and reduce the number of redundant handovers.

The handover algorithms described in the above are based on the legacy handover technique where femtocells are considered as standalone cells with independent cell IDs. However, a physical-cell-identity (PCI) confusion must be resolved in SCNs if the same PCIs are reused in the networks. Moreover, it is inefficient to apply the traditional handover technique to a virtual-cell network because the traditional handover technique was designed for an X2 interface network, while there is no X2 interface connection in the virtual cells in the same vicinity of the eNodeB. Therefore, an efficient handover technique needs to be developed for SCNs that are virtually generated by the eNodeB with 3D beamforming.

Traditional LTE synchronization signals, the primary synchronization signal (PSS) and secondary synchronization signal (SSS), can support up to 504 PCIs [19]. In addition, orthogonal sequences such as the Hadamard sequence and polyphase sequence can be used to provide an interference-free signal transmission (zero autocorrelation) [20]. However, the number of sequences that can be generated by an orthogonal sequence is usually limited by the sequence length. Thus, if an orthogonal sequence is used for the SCN that requires a large set of synchronization signals, PCI confusion may occur. On the other hand, non-orthogonal sequences such as the Gold sequence and pseudorandom sequence can be used to generate a large set of sequences. However, they are known to have poor correlation and high peak-to-average power ratio (PAPR). Because they are not designed in a hierarchical manner, the computational complexity required for cell searching in a virtual-cell network will be high. In Section III, we describe a synchronization signal appropriate for SCNs that are virtually generated by the eNodeB with 3D beamforming.

3. VIRTUAL-CELL SYNCHRONIZATION SIGNAL

Figure 1 shows two different deployment scenarios for SCNs with 3D beamforming: terrestrial deployment and balloon-based deployment. Figure 1(a) shows a terrestrial SCN where each eNodeB is equipped with a 3D beamformer. In Figure 1(b), the 3D beamformer is attached to the bottom of a balloon in the sky. In Figure 1, each cell is split into many virtual cells by means of 3D beamforming. A cell and virtual cell are assigned with a MCID and VCID, respectively.

In this section, we focus on the design of a VCSS suitable for a next-generation LTE system, assuming that the MCID is carried by the conventional PSS and SSS. It is assumed that one additional OFDM symbol, transmitted next to the SSS, is inserted in a frame to carry the VCID. The OFDM symbol, referred to as the VCSS in this paper, needs to carry the MCID as well as the VCID because the VCID needs to be detected in a multi-cell environment. If the VCSS carries only the VCID information, it will not be possible to determine which macrocell transmitted the VCSS. Therefore, the information (both the MCID and VCID), assigned to the virtual cell, should be transmitted in the VCSS. However, a large number of different sequences (MCID × VCID) are needed to transmit the information in the synchronization signal. In order to transmit the information in one OFDM symbol, the proposed VCSS is designed such that the VCID is mapped to the sequence in association with its MCID. The proposed VCSS can be viewed as a combination of a Chu sequence and polyphase sequence [20]. Depending on the ID mapping scheme, we propose two different types of VCSSs. In the first type of VCSS (Type-1), a signal is generated by mapping the MCID to the root index of a Chu sequence and the VCID to the index of a polyphase sequence. In the second type of VCSS (Type-2), a signal is generated by mapping the MCID to the index of a polyphase sequence and the VCID to the root index of a Chu sequence. These two sequences (Type-1 and Type-2) are proposed for

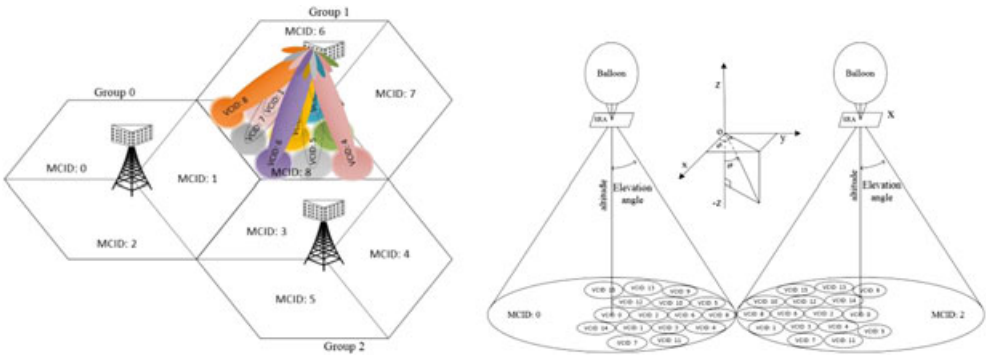

(a) Terrestrial SCN (b) Balloon-based SCN

Figure 1. Deployment scenarios for SCNs with 3D beamforming.

the VCSS because they satisfy the following requirements. First, they allow us to design the synchronization signal in a hierarchical manner. Second, a minimal change is required from the current LTE specification. Note that the basic sequence used for the VCSS in this paper is a prime-length Zadoff–Chu sequence used in the PSS in the LTE system. Third, they possess correlation properties required for the synchronization signal. The properties of Type-1 and Type-2 sequences will be explained in the following.

A Type-1 VCSS is defined by the multiplication of a prime-length Chu sequence $X^{c_b}(k)$ and a polyphase sequence $P^{Lv_i}(k)$ in the frequency domain, as follows:

$$\begin{aligned} X^{c_b,v_i}(k) &= X^{c_b}(k)P^{Lv_i}(k) \\ X^{c_b}(k) &= e^{j\frac{\pi r_{c_b}k(k+1)}{N}},\ P^{Lv_i}(k) = e^{-j\frac{2\pi Lv_ik}{N}} \end{aligned} \tag{1}$$

where $c_b \in \mathbb{N}_C$, $v_i \in \mathbb{N}_V$, and $r_{c_b} \in \mathbb{N}_R$ denote the MCID of the b-th eNodeB, VCID of the i-th virtual cell, and Chu 's root index mapped with MCID c_b, respectively. $\mathbb{N}_C = \{0 \quad 1 \quad \cdots \quad N_C-1\}$, $\mathbb{N}_V = \{0 \quad 1 \quad \cdots \quad N_V-1\}$, and $\mathbb{N}_R = \{1 \quad 2 \quad \cdots \quad N_R\}$ denote the set of MCIDs, set of VCIDs, and set of all possible Chu's root indices, respectively. N_C, N_V, N_R, and N denote the number of MCIDs, number of VCIDs in each cell, number of all possible Chu's root indices, and sequence length, respectively. N_R is given by $N-1$, and k denotes the subcarrier number in the frequency domain. The parameter L in (1) is inserted to avoid the incorrect detection of cell ID when a symbol timing error exists. The value of L must be increased in proportion to the symbol timing error because of the time delay between the eNodeB and UE. Scaling the phase part, $-2\pi v_i k/N$, by parameter L results in a reduction in the number of VCIDs. The maximum number of VCIDs is reduced to $\lfloor N/L \rfloor$, where $\lfloor \cdot \rfloor$ denotes the floor operation. The amplitude of the VCSS in the time domain, and its autocorrelation function in the frequency domain, are given by

$$\begin{aligned} x^{c_b,v_i}(n) &= x^{c_b}(0)X^{c_b}{}^*\left(r_{c_b}^{-1}(n-Lv_i)\right) \\ x^{c_b}(0) &= \frac{1}{\sqrt{N}}\left(\frac{\alpha r_{c_b}}{N}\right)\frac{1-j^N}{1-j}e^{-j\frac{2\pi r_{c_b}\alpha\gamma^2}{N}} \end{aligned} \tag{2}$$

$$\begin{aligned} R^{c_b,v_i}(l) &= \sum_{k=0}^{N-1} X^{c_b,v_i}(k)X^{c_b,v_i}{}^*(k+l) \\ &= \sum_{k=0}^{N-1} e^{j\frac{\pi(r_{c_b}l(l+1)-2Lv_il)}{N}} e^{j\frac{2\pi r_{c_b}kl}{N}} \\ &= Ne^{j\frac{\pi(r_{c_b}l(l+1)-2Lv_il)}{N}}\delta(\mathrm{mod}(l,N)) \end{aligned} \tag{3}$$

where $r_{c_b}^{-1}$ and $\delta(\cdot)$ denote the multiplicative inverse of r_{c_b} and Kronecker delta function, respectively. $(\alpha r_{c_b}/N)$ denotes the Legendre symbol, which has a value of -1, 0, or 1, with $\alpha=(N+1)/2$ and $\gamma=(N-1)/2$. As seen in (2) and (3), the time-domain version of Type-1 VCSS, $x^{c_b,v_i}(n)$, has a constant amplitude and zero autocorrelation except at the lag l where $\mathrm{mod}(l,N)=0$, satisfying the CAZAC property. The CAZAC property of Type-1 VCSS can be proved using the inverse discrete Fourier transform (IDFT) property of Zadoff–Chu sequence [21,22]. This property holds for the VCSS generated by combining either an even- or odd-length Chu sequence with a polyphase sequence in the same manner as in (1) if the Chu 's root index and its length are co-prime. Intra-cell correlation (defined as the correlation between two virtual cells v_0 and v_i in the same cell) and inter-cell correlation (defined as the correlation between a virtual cell in one cell and a virtual cell in another cell) are given in an ideal condition (where channel and noise effects are ignored) when the Chu sequence is of prime length, as follows:

$$\begin{aligned} R_1^{c_0,c_0}(v_0,v_i) &= \sum_{k=0}^{N-1} X^{c_0,v_i}(k)X^{c_0,v_0}{}^*(k) \\ &= \sum_{k=0}^{N-1} e^{j\frac{2\pi kL(v_0-v_i)}{N}} = N\delta(v_0-v_i) \end{aligned} \tag{4}$$

$$\begin{aligned} R_1^{c_0,c_b}(v_0,v_i) &= \sum_{k=0}^{N-1} X^{c_b,v_i}(k)X^{c_0,v_0}{}^*(k) = \sum_{k=0}^{N-1} e^{j\frac{\pi r_{c_bc_0}k(k+1)}{N}} e^{j\frac{2\pi kL(v_0-v_i)}{N}} \\ &= e^{-j\frac{\pi r_{c_bc_0}r_{c_bc_0}^{-1}L(v_0-v_i)\left(r_{c_bc_0}^{-1}L(v_0-v_i)+1\right)}{N}} \sum_{k=0}^{N-1} e^{j\frac{\pi r_{c_bc_0}k(k+1)}{N}} \\ &= \Sigma^{c_b,c_0} e^{-j\frac{\pi r_{c_bc_0}r_{c_bc_0}^{-1}L(v_0-v_i)\left(r_{c_bc_0}^{-1}L(v_0-v_i)+1\right)}{N}} \end{aligned} \tag{5}$$

where

$$\begin{aligned} \Sigma^{c_b,c_0} &= \sum_{k=0}^{N-1} e^{j\frac{\pi r_{c_bc_0}k(k+1)}{N}} \\ &= \sqrt{N}\begin{cases} \left(\frac{\alpha|r_{c_bc_0}|}{N}\right)\frac{1-j^N}{1-j}e^{-j\frac{2\pi r_{c_bc_0}\alpha\gamma^2}{N}}, & r_{c_b} > r_{c_0} \\ \left(\frac{\alpha|r_{c_bc_0}|}{N}\right)\frac{1+j^N}{1+j}e^{-j\frac{2\pi r_{c_bc_0}\alpha\gamma^2}{N}}, & r_{c_b} < r_{c_0} \end{cases} \end{aligned} \tag{6}$$

Here, the subscript 1 indicates the Type-1 VCSS. In addition, $r_{c_b c_0}^{-1}$ denotes the multiplicative inverse of $r_{c_b c_0}$, where $r_{c_b c_0} = r_{c_b} - r_{c_0}$. (5) can be derived using the Gauss sum expression [23]. Note that the amplitude of the inter-cell correlation is $\sqrt{N}$, and the intra-cell correlation has a peak only when $v_0 = v_i$ for $v_0, v_i \in \mathbb{N}_V$. As seen in (4) and (5), the VCSSs with the same Chu's root indices are perfectly orthogonal whereas the VCSSs with different Chu's root indices are not orthogonal. This property is referred to as a subset-orthogonality property in this paper because the orthogonality property holds true only for a subset of VCSSs that have the same Chu's root index.

The Type-2 VCSS is defined by the multiplication of a Chu sequence $X^{v_i}(k)$ and polyphase sequence $P^{c_b L}(k)$ in the frequency domain, as follows:

$$X^{c_b, v_i}(k) = X^{v_i}(k) P^{c_b L}(k). \tag{7}$$

For a Type-2 VCSS, the intra-cell correlation and inter-cell correlation are given as follows:

$$R_2^{c_0,c_0}(v_0, v_i) = \begin{cases} N, & v_0 = v_i \\ \Sigma^{v_i, v_0}, & v_0 \neq v_i \end{cases}$$
$$R_2^{c_0,c_b}(v_0, v_i) = \begin{cases} 0, & v_0 = v_i \\ \Sigma^{v_i, v_0} e^{-j\frac{\pi r_{v_i v_0} r_{v_i v_0}^{-1} L(c_0 - c_b)\left(r_{v_i v_0}^{-1} L(c_0 - c_b) + 1\right)}{N}}, & v_0 \neq v_i \end{cases}. \tag{8}$$

Here, the subscript 2 indicates the Type-2 VCSS. In addition, $r_{v_i v_0} = r_{v_i} - r_{v_0}$. The Type-2 VCSS will have a non-zero intra-cell correlation when an incorrect VCID is selected, and a non-zero inter-cell correlation except in the case where two VCSSs from two different cells have the same Chu's root indices.

Next, we compare the properties of two different types of VCSSs. First, the parameter L for a Type-2 VCSS is usually set to be larger than that of a Type-1 VCSS because the time delay (distance) between two different cells is usually larger than the delay (distance) between two virtual cells in the same cells. In other words, the cardinality of the set of a Type-1 VCSS is larger than that of a Type-2 VCSS.

Second, an interference metric (IM) is defined to measure the interference from the virtual cells in all the neighboring cells. This IM can be derived by subtracting the effect of the serving virtual cell from the total correlation value. The upper bound of the IM can be derived as follows:

$$\left|\boldsymbol{IM}_1^{c_0,v_0}\right| = \left|\sum_{b=0, c_b \neq c_0}^{N_B-1} \sum_{i=0}^{N_I-1} R_1^{c_0,c_b}(v_0, v_i)\right| \leq \sqrt{N}(N_B - 1)N_I$$
$$\left|\boldsymbol{IM}_2^{c_0,v_0}\right| = \left|\sum_{i=0, v_i \neq v_0}^{N_I-1} R_2^{c_0,c_0}(v_0, v_i) + \sum_{b=0, c_b \neq c_0}^{N_B-1} \sum_{i=0, v_i \neq v_0}^{N_I-1} R_2^{c_0,c_b}(v_0, v_i)\right| \tag{9}$$
$$\leq \sqrt{N} N_B (N_I - 1)$$

where $N_B (\leq N_C)$ and $N_I (\leq N_V)$ denote the number of neighboring cells and number of neighboring virtual cells affecting the UE in the serving virtual cell, respectively. In the case of a single-cell environment ($N_B = 1$ and $N_I > 1$), $\max\left|\boldsymbol{IM}_1^{c_0,v_0}\right| = 0$ for a Type-1 VCSS, and $\max\left|\boldsymbol{IM}_2^{c_0,v_0}\right| = \sqrt{N}(N_I - 1)$ for a Type-2 VCSS. In the case of a multi-cell environment, the IM of a Type-1 VCSS is smaller than that of a Type-2 VCSS because N_I is usually greater than N_B. Note that the coverage of a virtual cell is much smaller than that of the eNodeB. The neighboring cells affecting the serving virtual cell are usually located farther away from the neighboring virtual cells. For example, the maximum IMs of Type-1 and Type-2 VCSSs, normalized by $\sqrt{N}$, are found to be 36 and 51, respectively, when $N_B = 3$ and $N_I = 18$. Therefore, the Type-1 VCSS is usually less affected by interference from the neighboring virtual cells.

Third, the computational complexities required for complete cell detection (both MCID and VCID) are compared for different synchronization signals. Table I compares the number of complex multiplications required for the proposed VCSSs and LTE signal. In the LTE case (PSS + SSS), it is assumed that the cell IDs carried by the PSS and SSS are assigned to virtual cells to identify small cells. It is also assumed that there are 504 small cells to avoid PCI confusion in this example. The result in Table I corresponds to the case of non-coherent detection for cell searching, ignoring the computational complexity for channel estimation and compensation [24]. In the proposed approach, the MCID is carried by the PSS and SSS, and the VCID is carried by the VCSS in a hierarchical manner.

In order to compare this with the LTE case, the parameters are set to $N = N_V = 71$, $L = 1$, and $N_C = 7$. With these parameters, it is possible to generate 497 ($\lfloor N_V / L \rfloor \times N_C$) different VCSSs, which is close to the number of small cells (504) in the LTE case. Although we can generate a larger number of VCSSs without PCI confusion, we use the parameters to make a comparison with the LTE case in this example. Using the inherent characteristic of the polyphase part in the VCSS, an inverse fast Fourier transform (IFFT) operation is applied to the detection of the VCID to reduce the computational complexity in the process of calculating the correlation. The logarithm term in the table corresponds to the complexity of the IFFT operation. In addition, $\lceil \cdot \rceil$ denotes the ceiling operation.

Table I. Comparison of number of complex multiplications required for complete cell identification.

	Number of complex multiplications	Examples
LTE (PSS + SSS)	62(504/3 + 4)	10,664
(PSS + SSS) + Type-2 VCSS	$62(N_C/3 + 4) + N + \lceil L\log_2 N/2 \rceil + NN_V$	5508
(PSS + SSS) + Type-1 VCSS	$62(N_C/3 + 4) + N + \lceil M\log_2 N/2 \rceil$	724

As seen by the results listed in this table, the Type-1 VCSS has the smallest number of complex multiplications.

4. EFFICIENT HANDOVER MEASUREMENT TECHNIQUE USING VCSS

The received signal at the UE in an OFDM system can be expressed as

$$\begin{aligned} Y(k) &= \sum_{b=0}^{N_B-1}\sum_{i=0}^{N_I-1}\sqrt{G^{c_b,v_i}}H^{c_b,v_i}(k)X^{c_b,v_i}(k) + Z(k) \\ &= \underbrace{\sum_{i=0}^{N_I-1}\sqrt{G^{c_0,v_i}}H^{c_0,v_i}(k)X^{c_0,v_i}(k)}_{\textit{Desired cell}} \\ &\quad + \underbrace{\sum_{b=0,c_b\neq c_0}^{N_B-1}\sum_{i=0}^{N_I-1}\sqrt{G^{c_b,v_i}}H^{c_b,v_i}(k)X^{c_b,v_i}(k)}_{\textit{Interfering cells}} + Z(k) \end{aligned} \tag{10}$$

where $X^{c_b,v_i}(k)$ denotes the VCSS transmitted from the i-th virtual cell with VCID v_i in the b-th cell with MCID c_b, at the k-th subcarrier. Here, c_0 denotes the MCID of the serving cell. In addition, G^{c_b,v_i} denotes the gain of a 3D beamformer in the direction of the i-th virtual cell from the b-th eNodeB, and $H^{c_b,v_i}(k)$ denotes the channel frequency response between eNodeB and UE when a beam is formed. In addition, $Z(k)$ denotes an additive white Gaussian noise (AWGN) in the frequency domain.

The complete cell detection is performed using the MCID and VCID estimated from synchronization signals. Here, we will focus on the detection of the VCID assuming that the initial synchronization and estimation of MCID c_0 have been successfully performed using the received PSS and SSS. The VCID in the serving cell with the MCID of c_0 is estimated as follows:

$$\hat{v}_i = \begin{cases} \underset{v_i\in\mathbb{N}_V}{\text{argmax}} \sum_{m=0}^{L-1}\left|\boldsymbol{R}_{\boldsymbol{I}}^{c_0}(v_i,m)\right|^2, \textbf{\textit{Type 1}} \\ \underset{v_i\in\mathbb{N}_V}{\text{argmax}} \sum_{m=0}^{L-1}\left|\boldsymbol{R}_{\boldsymbol{2}}^{c_0}(v_i,m)\right|^2, \textbf{\textit{Type 2}} \end{cases} \tag{11}$$

where

$$\begin{aligned} \boldsymbol{R}_{\boldsymbol{I}}^{c_0}(v_i,m) &= \frac{1}{N}\sum_{k=0}^{N-1}Y(k)X^{c_0}{}^*(k)e^{j\frac{2\pi k(m+Lv_i)}{N}} \\ \boldsymbol{R}_{\boldsymbol{2}}^{c_0}(v_i,m) &= \frac{1}{N}\sum_{k=0}^{N-1}Y(k)X^{v_i}{}^*(k)e^{j\frac{2\pi k(m+Lc_0)}{N}}. \end{aligned} \tag{12}$$

Note that the notation $\boldsymbol{R}$ has a slightly different meaning from R in this paper. R is the correlation between two VCSSs, whereas $\boldsymbol{R}$ is the correlation between the received signal and the VCSS. In addition, the VCID in (11) is estimated by finding the value that maximizes the squared correlation summing over interval L because its detection probability can be improved by combining the effect of the multipath channel.

The detection probability of VCID for a Type-1 VCSS in a Rayleigh fading channel is given by [25]

$$P_{v_0} = \int_{\varsigma}^{\infty} f_{c_0}(r|\mathrm{H}_0)\left[\int_0^r f_{c_0}(z|\mathrm{H}_1)dz\right]^{N_V-1}dr \tag{13}$$

where $f_{c_0}(r|\boldsymbol{H}_0)$ and $f_{c_0}(r|\boldsymbol{H}_1)$ denote probability density functions of the decision random variable, $\left|\boldsymbol{R}_1^{c_0}(v_0)\right|^2$, under hypotheses $\boldsymbol{H}_0$ and $\boldsymbol{H}_1$, respectively. Here, the index m is omitted from the decision random variable because perfect timing is assumed. $\boldsymbol{H}_0$ and $\boldsymbol{H}_1$, are the hypotheses corresponding to a correct decision and incorrect decision made on a virtual cell, respectively. The parameter ς denotes a threshold value. Here, it is assumed that $N_V - 1$ decision random variables with hypothesis $\boldsymbol{H}_1$ are independent and identically distributed. Then, $f_{c_0}(r|\boldsymbol{H}_0)$ and $f_{c_0}(r|\boldsymbol{H}_1)$, which are two degree-of-freedom chi-square random variables, can be expressed as [26]

$$f_{c_0}(r|\boldsymbol{H}_0) = \frac{1}{\sigma_0^2}e^{\frac{-r}{\sigma_0^2}}, f_{c_0}(r|\boldsymbol{H}_1) = \frac{1}{\sigma_1^2}e^{\frac{-r}{\sigma_1^2}} \tag{14}$$

$$\sigma_0^2 = G^{c_0,v_0} + \sigma_c^2 + \sigma^2,\ \sigma_1^2 = \sigma_{c_0}^2 + \sigma_c^2 + \sigma^2 \tag{15}$$

where

$$\begin{aligned} \sigma_c^2 &= \frac{1}{N}\sum_{b=0,c_b\neq c_0}^{N_B-1}\sum_{i=0}^{N_I-1}G^{c_b,v_i} \\ \sigma_{c_0}^2 &= \frac{1}{N_I-1}\sum_{i=0,v_i\neq v_0}^{N_I-2}G^{c_0,v_i}. \end{aligned} \tag{16}$$

Here, σ^2 denotes the noise variance in the time domain. Substituting (14) into (13), one can obtain the detection probability of the VCID as follows:

$$P_{v_0} = \frac{1}{\sigma_0^2}\int_{\varsigma}^{\infty} e^{-\frac{r}{\sigma_0^2}} \left(\frac{1}{\sigma_1^2}\int_0^r e^{-\frac{z}{\sigma_1^2}} dz\right)^{N_V-1} dr = \sum_{i=0}^{N_V-1} \binom{N_V-1}{i} \frac{(-1)^i \sigma_1^2}{\sigma_1^2 + i\sigma_0^2} e^{-\frac{(\sigma_1^2 + i\sigma_0^2)\varsigma}{\sigma_0^2\sigma_1^2}}. \quad (17)$$

As seen in (17), the virtual-cell detection performance depends on the side-lobe levels of the beam pattern, which are transmitted from virtual cells in the serving cell and neighboring (interfering) cells, and the number of virtual cells, N_V. The detection probability of a complete cell ID P_0 is given by multiplying the detection probability of the MCID and the detection probability of the VCID in (17). That is, $P_0 = P_{c_0}P_{v_0}$ where $P_{c_0} = P_{\boldsymbol{PSS}}P_{\boldsymbol{SSS}}$. Here, P_{c_0}, $P_{\boldsymbol{PSS}}$, and $P_{\boldsymbol{SSS}}$ denote the detection probabilities of the MCID, PSS, and SSS, respectively. The detection probability has only been described for virtual cells because the detection probabilities of PSS and SSS in the LTE system are well studied in the literature.

In SCNs, handover events occur more frequently because of the small cell size. If the LTE-based handover technique is applied to SCNs, it will increase the handover overhead which includes the signaling overhead and latency. In SCNs, the overhead required for intra-cell handover can be significantly reduced because no X2 interface connection is needed for virtual cells in the vicinity of the same eNodeB. However, it is not possible to distinguish an intra-cell handover from an inter-cell handover using the received synchronization signals in the LTE system. The UE in the LTE system cannot determine whether the target virtual cell is within the coverage of the serving eNodeB or that of another eNodeB. However, with the synchronization signals of the hierarchical structure in the proposed approach, the UE can determine whether the UE is inside or outside of a serving virtual cell and whether the UE is inside or outside of a serving cell. Based on the measurement report obtained by the VCSS, the eNodeB can distinguish an intra-cell handover from an inter-cell handover. In the case of an intra-cell handover, several steps required by traditional LTE systems can be skipped in SCNs, resulting in a significant reduction in the processing time. The signal metrics that can be used for the intra-cell/inter-cell handover decision are defined using (12), as follows:

$$S_V^{c_b,v_i} = \sum_{m=0}^{L-1} \left|\boldsymbol{R}_j^{c_b}(v_i,m)\right|^2$$
$$S_M^{c_b} = \sum_{i=0}^{N_I-1}\sum_{m=0}^{L-1} \left|\boldsymbol{R}_j^{c_b}(v_i,m)\right|^2, j = \{1,2\} \quad (18)$$

where $S_M^{c_b} \in \mathrm{S}_M$ and $S_V^{c_b,v_i} \in \mathrm{S}_V^{c_b}$ denote signal metrics for cell b and virtual cell i in cell b, respectively. $\mathrm{S}_M = \left\{S_M^{c_0}, S_M^{c_1}, \cdots, S_M^{c_{N_B-1}}\right\}$ and $\mathrm{S}_V^{c_b} = \left\{S_M^{c_b,v_0}, S_M^{c_b,v_1}, \cdots, S_M^{c_b,v_{N_I-1}}\right\}$ denote a set of signal metrics for N_B neighboring cells and a set of signal metrics for N_I neighboring virtual cells in cell b, respectively. Figures 2 and 3 show the proposed handover technique and decision-making process using the signal metrics in (18), respectively. In Figure 2, $\mathbb{N}_B = \{c_0, c_1, \cdots, c_{N_B-1}\}$ and $\mathbb{N}_I = \{v_0, v_1, \cdots, v_{N_I-1}\}$ denote a set of MCIDs of neighboring cells and a set of VCIDs of neighboring virtual cells, respectively. The terms MME, S-GW, and RACH stand for the mobile management entity, serving gateway, and random access channel, respectively. The flowchart in Figure 2 is a simplified version of the handover technique. For example, the flow of the user's packet data and the data flow between a serving cell and target cell are not shown in the figure. As seen in Figure 2, there is no signaling between the serving cell and target cell or between the MME and S-GW in the intra-cell handover case. The dashed lines in the intra-cell handover indicate optional steps for acquiring synchronization parameters, such as timing offset, frequency offset, and timing advanced information. In SCNs with 3D beamforming, virtual cells are simultaneously generated by each eNodeB with a set of 3D beams. Thus, a network of virtual cells within the vicinity of an eNodeB can be regarded as a synchronous network. Time and frequency synchronization may not be required in a virtual-cell network. The synchronization parameters obtained from the serving virtual cell can be applied to the target cell in the intra-cell handover case. However, in SCNs with distributed radio units, the UE in the intra-cell handover may need to perform both synchronization and random access because of their different channel environments. As seen in this figure, many signaling steps can be skipped in the case of an intra-cell handover, which implies that a significant reduction in the signaling overhead can be obtained.

Figure 3 shows the decision conditions for an intra-cell/inter-cell handover. If $S_M^{c_0} + \varsigma_M < S_M^{c_T}$ and $S_V^{c_0,v_0} + \varsigma_V < S_V^{c_T,v_T}$, a decision is made for an inter-cell handover. If $S_M^{c_0} + \varsigma_M > S_M^{c_T}$ and $S_V^{c_0,v_0} + \varsigma_V < S_V^{c_T,v_T}$, a decision is made for an intra-cell handover. Here, ς_M and ς_V denote hysteresis margins for macro- and virtual-cell handovers, respectively, which are inserted to prevent a ping-pong effect. In addition, $c_0 \in \mathbb{N}_B$, $c_T \in \mathbb{N}_B$, $v_0 \in \mathbb{N}_I$, and $v_T \in \mathbb{N}_I$ denote the serving MCID, target MCID, serving VCID, and target VCID, respectively.

Next, the statistical properties of the metrics in (18) are derived for a Rayleigh fading channel. The mean and variance of the signal metric $S_V^{c_b,v_i}$ can be derived as follows:

$$\boldsymbol{E}[S_V^{c_b,v_i}] = \sigma_{c_b,v_i}^2$$
$$\boldsymbol{Var}[S_V^{c_b,v_i}] = \boldsymbol{E}\left[\left(S_V^{c_b,v_i}\right)^2\right] - \boldsymbol{E}^2[S_V^{c_b,v_i}] = \sigma_{c_b,v_i}^4 \quad (19)$$

where

$$\sigma_{c_b,v_i}^2 = \begin{cases} G^{c_b,v_i} + \frac{1}{N_{j=0,j\neq b}} \sum^{N_B-1} \sum_{i=0}^{N_I-1} G^{c_j,v_i} + \sigma^2 & , \textbf{\textit{Type 1}} \\ G^{c_b,v_i} + \frac{1}{N}\left(\sum_{l=0,l\neq i}^{N_I-1} G^{c_b,v_l} + \sum_{j=0,j\neq bl=0,l\neq i}^{N_B-1}\sum^{N_I-1} G^{c_j,v_l}\right) + \sigma^2 & , \textbf{\textit{Type 2}} \end{cases}. \quad (20)$$

Note that the effect of the beamforming gain in the serving virtual cell of the serving cell is included in (20).

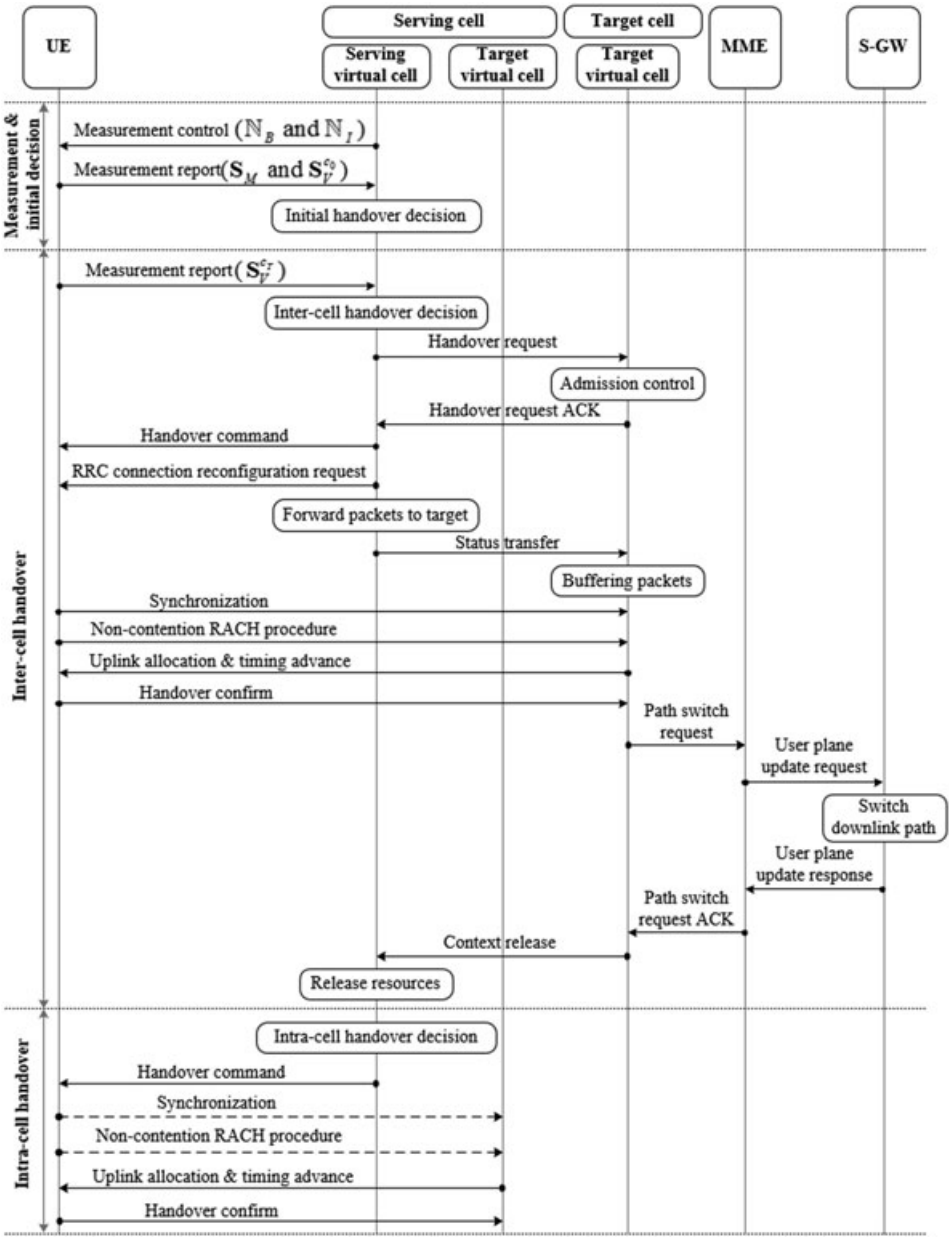

Figure 2. Proposed handover technique for SCNs.

The effect of the sidelobes transmitted from virtual cells in the neighboring cells is included in the Type-1 VCSS. The effect of the sidelobes transmitted from virtual cells in the serving cell and from virtual cells in the neighboring cells (except the case where two VCSSs from two different cells have the same MCID) is included in the Type-2 VCSS. When $\sigma^2_{c_b,v_0} \neq \sigma^2_{c_b,v_1} \neq \cdots \neq \sigma^2_{c_b,v_{N_I-1}}$, the PDF of the signal metric $S_M^{c_b}$ can be expressed as follows [27]:

$$f_{S_M^{c_b}}(s) = \sum_{i=0}^{N_I-1} \frac{e^{-\frac{s}{\sigma^2_{c_b,v_i}}}}{\sigma^2_{c_b,v_i} \prod_{j=0,j\neq i}^{N_I-1} \left(1 - \frac{\sigma^2_{c_b,v_j}}{\sigma^2_{c_b,v_i}}\right)}. \quad (21)$$

Then, the mean and variance of $S_M^{c_b}$ can be derived as follows:

$$\boldsymbol{E}[S_M^{c_b}] = \int_0^\infty s f_{S_M^{c_b}}(s) ds = \sum_{i=0}^{N_I-1} \frac{\sigma^2_{c_b,v_i}}{\prod_{j=0,j\neq i}^{N_I-1} \left(1 - \frac{\sigma^2_{c_b,v_j}}{\sigma^2_{c_b,v_i}}\right)}, \quad (22)$$

$$\boldsymbol{Var}[S_M^{c_b}] = \boldsymbol{E}\left[(S_M^{c_b})^2\right] - \boldsymbol{E}^2[S_M^{c_b}], .$$

$$\boldsymbol{E}\left[(S_M^{c_b})^2\right] = \int_0^\infty s^2 f_{S_M^{c_b}}(s) ds = \sum_{i=0}^{N_I-1} \frac{2\sigma^4_{c_b,v_i}}{\prod_{j=0,j\neq i}^{N_I-1} \left(1 - \frac{\sigma^2_{c_b,v_j}}{\sigma^2_{c_b,v_i}}\right)} \quad (23)$$

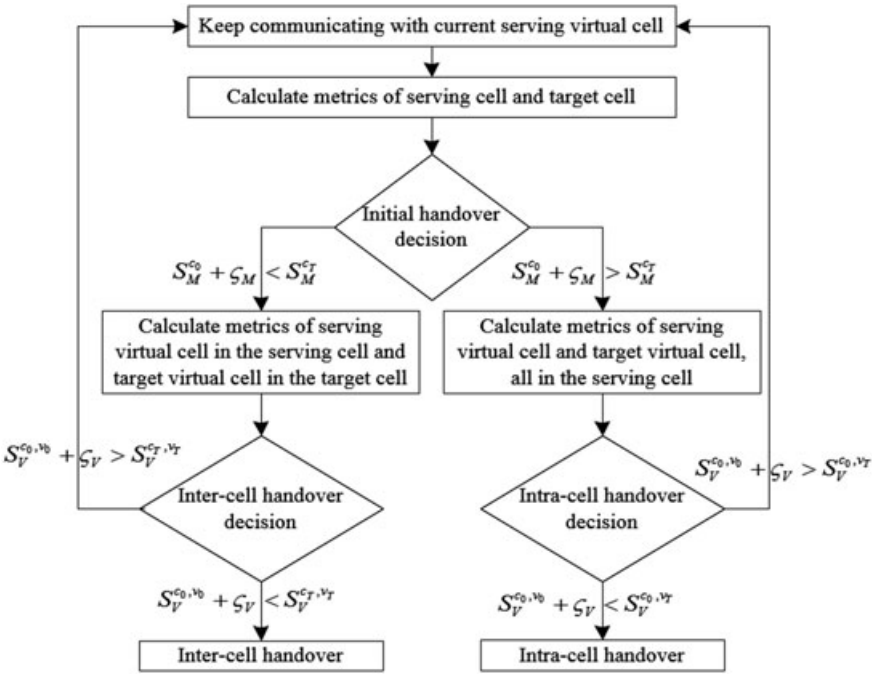

Figure 3. Proposed decision-making process for SCNs.

When $\sigma^2_{c_b,v_0} = \sigma^2_{c_b,v_1} = \cdots = \sigma^2_{c_b,v_{N_I-1}}$, the mean and variance of the signal metrics of $2N_I$ degree-of-freedom chi-square random variables are given by

$$\begin{aligned} \boldsymbol{E}[S_M^{c_b}] &= N_I \sigma^2_{c_b,v_i} \\ \boldsymbol{Var}[S_M^{c_b}] &= N_I \sigma^4_{c_b,v_i}. \end{aligned} \tag{24}$$

The mean and variance of the signal metric in (19)–(24) can be used to predict the behavior of signal metric in a SCN and to provide the region where an intra-cell/inter-cell handover decision needs to be made.

5. SIMULATION

In this section, the performance of the proposed handover measurement technique with the VCSS is evaluated in SCNs constructed using eNodeBs with 3D beamforming. The two different deployment cases in Figure 1 are considered. Only the performances of two adjacent cells ($N_B = 2$) are evaluated to simplify the simulation. The inter-site distance between two cells is set to 100 m for the terrestrial SCN in Figure 1(a) and 3 km for the balloon-based SCN in Figure 1(b). In the balloon-based SCN scenario, each balloon is assumed to fly at an altitude of 1 km. The frame structure and related parameters for signal transmission are based on LTE specifications [28,29]. The sequence lengths of the VCSSs are all set to 71, which is smaller than the number of subcarriers supported by the minimum bandwidth in the LTE system. Thus, the bandwidth allocated to the VCSS is compatible with the bandwidth in LTE systems. The only difference from the LTE specifications is the additional VCSS transmitted next to the SSS every 5 ms.

The standard rectangular array (SRA) is used for 3D beamforming at the eNodeB. The square of a normalized beam pattern, or simply the normalized beamforming gain of the SRA, is given by [30,31]

$$G^{c_b,v_i} = \left(\frac{\operatorname{sinc}\left(M_x\left(\psi_x - \psi_x^{c_b,v_i}\right)\right)}{\operatorname{sinc}\left(\psi_x - \psi_x^{c_b,v_i}\right)} \cdot \frac{\operatorname{sinc}\left(M_y\left(\psi_y - \psi_y^{c_b,v_i}\right)\right)}{\operatorname{sinc}\left(\psi_y - \psi_y^{c_b,v_i}\right)} \right)^2 \tag{25}$$

where

$$\begin{aligned} &\psi_x = \frac{\pi}{2} u_x, \psi_y = \frac{\pi}{2} u_y, \psi_x^{c_b,v_i} = \frac{\pi}{2} u_x^{c_b,v_i}, \ \psi_y^{c_b,v_i} = \frac{\pi}{2} u_y^{c_b,v_i}, \\ &u_x = \sin\theta\cos\phi, u_y = \sin\theta\sin\phi, \\ &u_x^{c_b,v_i} = \sin\theta_{tilt}^{c_b,v_i}\cos\phi_{tilt}^{c_b,v_i}, \psi_y^{c_b,v_i} = \sin\theta_{tilt}^{c_b,v_i}\sin\phi_{tilt}^{c_b,v_i}. \end{aligned} \tag{26}$$

In the balloon-based SCN scenario, it is assumed that the array is located in the xy plane and that the direction of the array (boresight) is opposite to the z direction, as can be seen in Figure 1(b). However, in the terrestrial SCN scenario, it is difficult to obtain a similar virtual cell coverage for virtual cells in the same cell using a single SRA because the height of the eNodeB is usually low compared with the cell coverage. Here, it is assumed that the height of the eNodeB is 30 m, and each eNodeB is equipped with three SRAs to form beams in the direction

of different elevation angles, as can be seen in Figure 4(a). In this case, the arguments of (25) are slightly modified, as follows:

$$\psi_x - \psi_x^{c_b,v_i} = \frac{\pi}{2}\left(\sin\left(\theta + \theta_{tilt}^{c_b,v_i} - \theta_0\right)\cos\phi - \sin\theta_0\cos\phi_{tilt}^{c_b,v_i}\right),$$
$$\psi_x - \psi_x^{c_b,v_i} = \frac{\pi}{2}\left(\sin\left(\theta + \theta_{tilt}^{c_b,v_i} - \theta_0\right)\sin\phi - \sin\theta_0\sin\phi_{tilt}^{c_b,v_i}\right), \quad (27)$$

where $\theta_{tilt}^{c_b,v_i}$ and $\phi_{tilt}^{c_b,v_i}$ denote the elevation tilting angle and azimuth tilting angle for virtual cell i in cell b, respectively. In addition, $\theta = \tan^{-1}(d/h)$, where d denotes the distance between the eNodeB and UE, and h denotes the height of the eNodeB. Here, θ_0, the elevation angle of a reference beam, is set to 65°. Figure 4 shows the 3D beam patterns when the SRA in (25) is used with the arguments in (26) and (27). In the terrestrial SCN scenario, three separate SRAs are used at each eNode. The first 5×5 SRA forms a single beam for the first tier. The second 7×7 SRA forms three beams for the second tier and the third 10×10 SRA forms five beams for the third tier. Figure 4(a) shows 18 virtual cells constructed by two eNodeBs with nine 3D beams each. In the balloon-based SCN scenario, a single 12×12 SRA is used at each balloon. Figure 4(b) shows 43 virtual cells constructed by one eNodeB with 43 3D beams. Here, the virtual cells constructed by only one balloon are shown.

Before applying the handover measurement technique to the SCN constructed by eNodeBs with 3D beamforming, the properties of the VCSS are verified under ideal conditions (where the channel and noise effects are ignored). Figure 5(a) and (b) shows the normalized squared magnitudes of the correlation values of Type-1 VCSSs and Type-2 VCSSs, respectively, when the sequence length N is 71 (prime number) and parameter L is 1. Here, a VCSS with MCID = 30 and VCID = 36 is selected as the sequence for the serving virtual cell. The number of all possible VCSSs is $N_C N_V = (N-1)\lfloor N/L \rfloor = 4970$ VCSSs for Type 1, and $N_C N_V = \lfloor N/L \rfloor (N-1)$

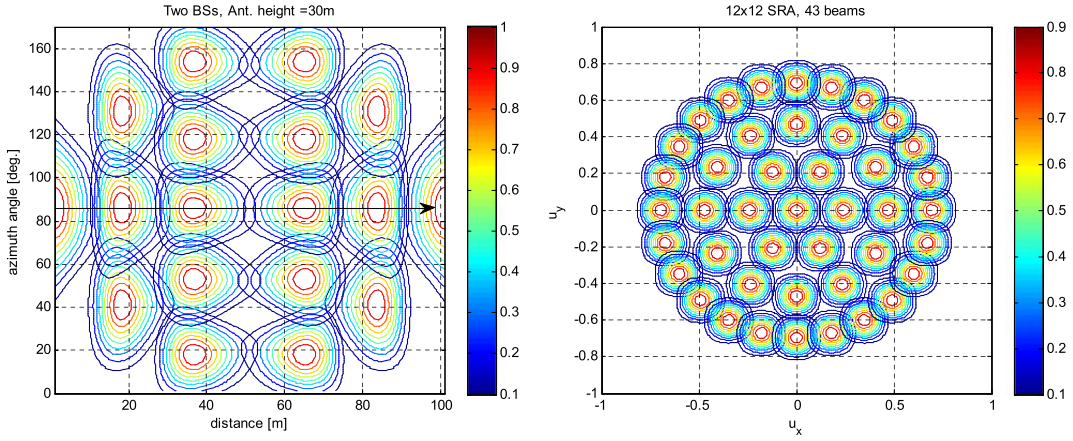

Figure 4. 3D beam patterns for two different cases of SCNs (top view).

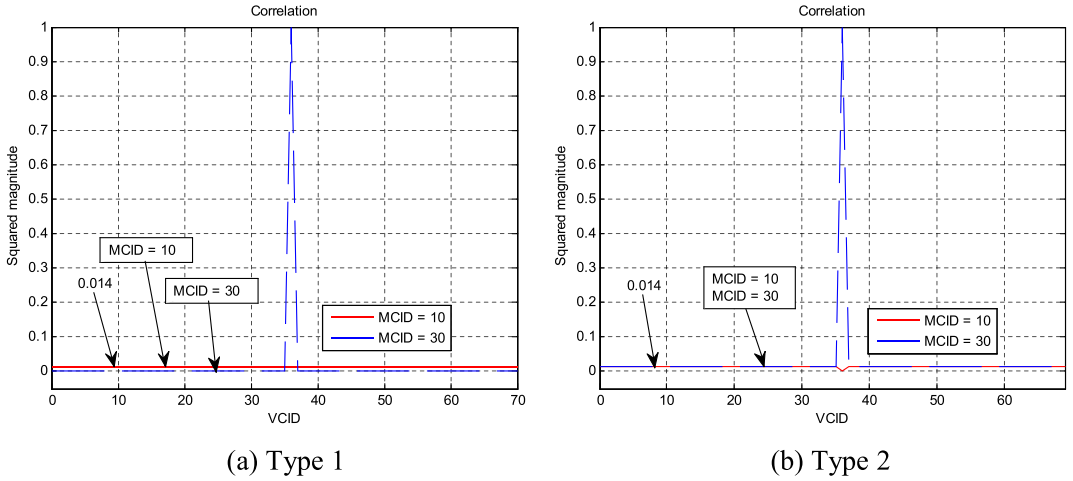

Figure 5. Correlation properties of VCSS.

= 4970 VCSSs for Type 2. The correlation values are normalized by the sequence length. As seen in Figure 5(a), the peak at MCID = 30 and VCID = 36 is 1. The intra-cell correlation values are equal to zero for all of the VCIDs except VCID = 36 when the sequence with MCID = 30 is used, as given by (4). In addition, the inter-cell correlation values are $\left|R_1^{c_0,c_b}(v_0,v_i)\right|^2/N^2(=1/N=0.014)$, $\forall c_b \neq c_0$, $v_0, v_i \in \mathbb{N}_V$, when the sequence with MCID = 10 is used, as given by (5) and (6). Therefore, the VCSSs in the same cell are orthogonal, and the VCSSs from the other cells are

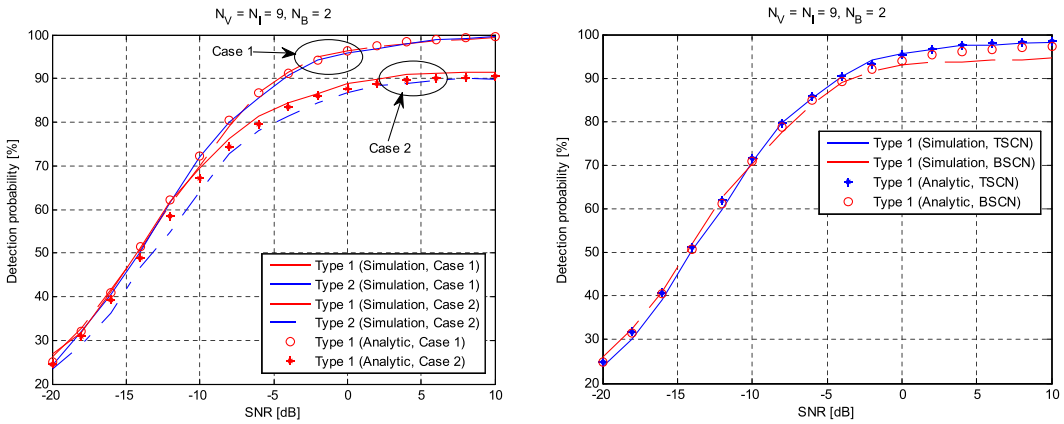

(a) SCN with same sidelobe levels (b) Two different SCN scenarios in Fig. 4

Figure 6. Detection probabilities of VCID in SCNs.

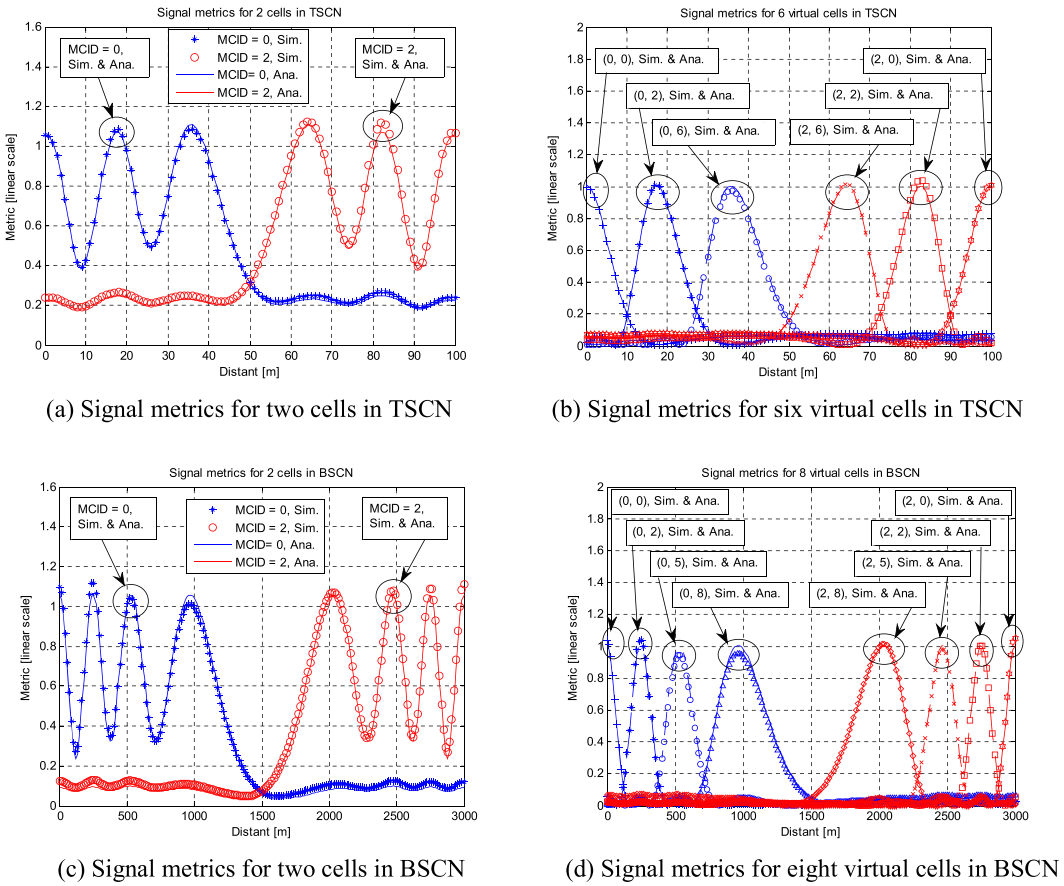

(a) Signal metrics for two cells in TSCN (b) Signal metrics for six virtual cells in TSCN

(c) Signal metrics for two cells in BSCN (d) Signal metrics for eight virtual cells in BSCN

Figure 7. Variation of signal metrics for two different SCN scenarios with 3D beamforming.

non-orthogonal when a Type-1 VCSS is used. As seen in Figure 5(b), the peak also exists at MCID = 30 and VCID = 36. However, the intra-cell correlation values are $\left|R_2^{c_0,c_0}(v_0,v_i)\right|^2/N^2(=0.014)$ at other VCIDs, which implies that the VCSSs in the same cell are non-orthogonal. The inter-cell correlation values are also $1/N(=0.014)$, $\forall\, c_b \neq c_0,\ v_i \neq v_0$ except in the case of a cell with the same Chu's root index (VCID = 36), as given by (8). Note that the cases with MCID = 10 and 30 are overlapped at all VCIDs except for the case with VCID = 36. In this case, the subset VCSSs using the same Chu's root indices are orthogonal sequences.

Figure 6 shows the detection probabilities of VCID when $N_V = N_I = 9, N_B = 2, \varsigma = 0$, and $N = 71$. The UE is assumed to receive nine signals from virtual cells in each cell and (11) is used to detect the VCID of the serving virtual cell in the simulation. In Figure 6(a), the simulation results are compared with the analytical results using (17) when the side-lobe levels of all the virtual cells are equal. Here, Case 1 corresponds to the case of a zero side-lobe level from interfering virtual cells, that is, $\sigma_{c_0}^2 = \sigma_c^2 = 0$. Case 2 corresponds to the case of non-zero side-lobe levels, that is, $\sigma_{c_0}^2 = 0.0203$ and $\sigma_c^2 = 0.016$. As seen in this figure, the simulation results obtained by the Type- and Type-2 VCSSs agree well with the analytical results using (17). Case 1 performs better than Case 2 because Case 2 has larger side-lobe levels. Case 2 also shows that a Type-1 VCSS (simulation) performs slightly better than a Type-2 VCSS (simulation) because of the smaller correlation value in the Type-1 VCSS. Figure 6(b) shows the simulation and analytical results for the two different scenarios of SCNs in Figure 4 when a Type-1 VCSS is used. Here, it is assumed that the UE is located at the center of the serving cell, that is, at the center of the virtual cell in the first tier of the terrestrial SCN (TSCN) and at $u_x = u_y = 0$ in the balloon-based SCN (BSCN). Because the side-lobe levels of all the virtual cells are different in these scenarios, the averaged values determined by (16) are used for the analytic case: $\sigma_{c_0}^2 = 0.0024$ and $\sigma_c^2 = 0.0016$ for TSCN, and $\sigma_{c_0}^2 = 0.0082$ and $\sigma_c^2 = 0.0008$ for BSCN. As seen in Figure 6 (b), the TSCN has a better detection probability than the BSCN because the BSCN has a higher $\sigma_{c_0}^2$.

Figure 7 shows the variation of the averaged signal metrics given in (18) for the two different SCN scenarios with 3D beam patterns in Figure 4. Here, the channel is assumed to experience Rayleigh fading, the SNR is set to 5 dB, and a Type-1 VCSS is used. In this figure, "Sim" and "Ana" stand for the simulation and analysis, respectively. In addition, the first and second parameters in parentheses represent the MCID and VCID values, respectively. Figure 7(a) and (b) shows the signal metrics for the terrestrial SCN scenario, where the UE is assumed to move between two cells in the direction of the arrow in Figure 4(a). Cell 1 is assigned an MCID

Table II. Processing time required for handover.

Step	Description	Conventional handover (ms)	Proposed handover	
			Inter-cell handover (ms)	Intra-cell handover (ms)
1	Measurement control (SVC to UE)	10	10	10
2	Measurement report (UE to SVC)	10	10	10
3	Handover decision (at SVC)	5	5	5
4	Handover request (SVC to TVC)	15	15	—
5	Admission control (at TVC)	20	20	—
6	Handover request ACK (TVC to SVC)	10	10	—
7	Handover command (SVC to UE)	20	20	20
8	RRC connection reconfiguration (SVC to UE)	10	10	—
9	Forward packets to target (at SVC)	5	5	—
10	Status transfer (SVC to TVC)	10	10	—
11	Buffering packets (at TVC)	5	5	—
12	Synchronization (UE to TVC)	10	10	—
13	Non-contention RACH procedure (UE to TVC)	20	20	—
14	Uplink allocation and timing advanced (TVC to UE)	10	10	10
15	Handover confirm (UE to TVC)	15	15	15
16	Path switch request (TVC to MME)	5	5	—
17	User plane update request (MME to S-GW)	5	5	—
18	Switch downlink path (at S-GW)	5	5	—
19	User plane update response (S-GW to MME)	5	5	—
20	Path switch request ACK (MME to TVC)	5	5	—
21	Context release (TVC to SVC)	10	10	—
22	Release resource (at SVC)	10	10	—
Total	Measurement control (SVC to UE)	220	220	70

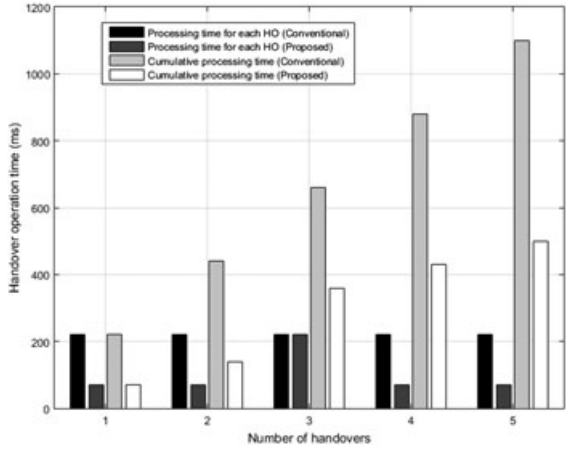

Figure 8. Processing time required for handover.

of 0, and cell 2 is assigned an MCID of 2. The UE passes through six virtual cells where three virtual cells for each cell are assigned VCID = {0, 2, 6}. Figure 7(a) shows the analytical results and simulation results for signal metrics $E\left[S_M^0\right]$ and $E\left[S_M^1\right]$. As seen in this figure, the analytical results obtained using (22) are similar to the simulation results. We can also easily detect the cell boundary by finding the crossing point of $E\left[S_M^0\right]$ and $E\left[S_M^1\right]$. Using the signal metrics, the serving cell can make a decision about an inter-cell handover to the target cell with an MCID of 2. Figure 7(b) shows the analytical results and simulation results for signal metrics $\boldsymbol{E}[S_V^{c_b,v_i}]$. As seen in this figure, the analytical results obtained using (19) are similar to the simulation results. We can also detect the virtual cell boundary by finding the crossing point of $\boldsymbol{E}[S_V^{c_b,v_i}]$. Two intra-cell handovers occur before the UE reaches the cell boundary. Therefore, the eNodeB can make an intra-cell/inter-cell handover decision based on the signal metrics in (18) and decision rule in Figure 3. Figure 7(c) and (d) shows the balloon-based SCN scenario. Similar results are obtained for this scenario.

Table II compares the processing times required for the conventional handover technique and proposed handover technique. In this table, TVC and SVC stand for the target virtual cell and serving virtual cell, respectively. As seen in this table, the processing time for the inter-cell handover in the proposed technique is the same as that for the conventional technique. However, the intra-cell handover significantly reduces the processing time because it can skip many steps required for an inter-cell handover. Figure 8 shows the cumulative processing time required for handovers in the terrestrial SCN scenario in Figure 4(a) as the number of handover events increases. For example, the total processing time required for handovers is 500 ms (four intra-cell handovers and one inter-cell handover) with the proposed technique, and 1100 ms (five inter-cell handovers) with the conventional technique.

6. CONCLUSION

In this paper, two different types of VCSSs were proposed for LTE-based SCNs that are virtually generated by 3D beamforming. The Type-1 VCSS was shown to be better suited for typical SCN deployment scenarios because it can produce a large set of cell IDs, is less affected by interference from neighboring virtual cells, and requires a small number of computations for cell detection. The proposed handover measurement technique was evaluated by computer simulation for terrestrial SCN and balloon-based SCN, which were both formed by SRAs. The signal metrics were shown to effectively detect cell boundaries or virtual cell boundaries by finding their crossing point, which allowed us to distinguish between an intra-cell handover and inter-cell handover in the SCNs. It was also shown that the total processing time for handover in the SCNs could be significantly reduced by the proposed handover measurement technique. Although this paper has focused on a SCN with 3D beamforming, the proposed technique could be applied to other types of SCNs because it does not depend on AAS or 3D beamforming algorithm. The processing time and signaling overhead for handover could be significantly reduced, especially when the SCN does not have an X2 interface connection or a group of small cells share a common baseband unit.

ACKNOWLEDGEMENTS

This research was supported by the Ministry of Science, ICT, and Future Planning (MSIP), Korea, under the Information Technology Research Center (ITRC) support program (IITP-2016-H8501-16-1007) supervised by the Institute for Information and Communications Technology Promotion (IITP), and by Basic Science Research Program through the National Research Foundation of Korea (NRF) funded by the Ministry of Education (2015R1D1A1A01057628).

REFERENCES

1. Andrews JG, Buzzi S, Choi W, Hanly SV, Lozano A, Soong AK, Zhang JC. What will 5G be? *IEEE Journal on Selected Areas in Communication* 2014; **32**(6): 1065–1082
2. Fehske AJ, Viering I, Voigt J, Sartori C, Redana S, Fettweis GP. Small-cell self-organizing wireless networks. *Proceedings of the IEEE* 2014; **102**(3): 334–350
3. Weitzen J, Mingzhe L, Anderland E, Eyuboglu V. Large-scale deployment of residential small cells. *Proceedings of the IEEE* 2013; **101**(11): 2367–2380
4. Ji H, Lee B, Shim B, Nam YH, Kwak Y, Noh H, Shin C. 3D beamforming for capacity boosting in LTE-advanced system. *PIMRC*: Hong Kong 2015; 2344–2348

5. Hardy H, Stephan S, Johannes K, Cornelis H. 3D beamforming: performance improvement for cellular networks. *Bell Labs Technical Journal* 2013; **18**(2): 37–56
6. Cheng X, Yu B, Yang L, Zhang J, Liu G, Wu Y, Wan L. Communication in the real world: 3D MIMO. *IEEE Wireless Communication Magazine* 2014; **21**(4): 136–144
7. Kuo PH. A glance at FD-MIMO technologies for LTE. *IEEE Wireless Communication* 2016; **23**(1): 2–5
8. Zhang Z, Teh KC, Li KH. Study of 3D beamforming strategies in cellular networks with clustered user distribution. *IEEE Transaction on Vehicular Technology* 2016. accepted for Publication.
9. Bladsjo D, Hogan M, Ruffini S. Synchronization aspects in LTE small cells. *IEEE Communication Magazine* 2013; **51**(9): 70–77
10. Xenakis D, Passas N, Merakos L, Verikoukis C. Mobility management for femtocells in LTE-advanced: key aspects and survey of handover decision algorithms. *IEEE Communication Surveys & Tutorials* 2014; **6**: 64–91
11. Yoo HI, Lee MN, Hong TH, Cho YS. A preamble design technique for efficient handover in IEEE 802.16-based mobile mesh networks. *IEEE Transaction on Vehicular Technology* 2013; **62**(1): 460–465
12. Lopez-Perez D, Valcarce A, Ladanyi A, Roche GDL, Zhang J. Intracell handover for interference and handover mitigation in OFDMA two-tier macrocell–femtocell networks. *EURASIP Journal on Wireless Communications and Networking* 2010; **01**: 1–15
13. Jeong B, Shin S, Jang I, Sung NW, Yoon H. A smart handover decision algorithm using location prediction for hierarchical macro/femto-cell networks. *VCT*: San Francisco 2011; 1–5
14. Rath A, Panwar S. Fast handover in cellular networks with femtocells. *ICC*: Ottawa 2012; 2752–2757
15. Zhang H, Ma W, Li W, Zheng W, Wen X, Jiang C. Signalling cost evaluation of handover management schemes in LTE-advanced femtocell. *VTC*: Budapest 2011; 1–5
16. Xenakis D, Passas N, Verikoukis C. A novel handover decision policy for reducing power transmissions in the two-tier LTE network. *ICC*: Ottawa 2012; 1352–1356
17. Moon J, Cho D. Efficient handover algorithm for inbound mobility in hierarchical macro/femto cell networks. *IEEE Communication Letters* 2009; **13**(10): 755–757
18. Xu P, Fang X, He R, Xing Z. An efficient handoff algorithm based on received signal strength and wireless transmission loss in hierarchical cell networks. *Telecommunication System* 2011; **52**(1): 317–325
19. Dahlman E, Parkvall S, Skold J. *4G LTE/LTE-Advanced for Mobile Broadband*. Elsevier: Oxford, 2011.
20. Zepernick HJ, Finger A. *Pseudo Random Signal Processing: Theory and Practice*. Wiley: Chichester, 2005.
21. Beyme S, Leung C. Efficient computation of DFT of Zadoff–Chu sequences. *Electronics Letters* 2009; **45**(9): 461–462
22. Popovic BM. Efficient DFT of Zadoff–Chu sequences. *Electronics Letters* 2010; **46**(7): 502–503
23. Berndt BC, Evans RJ, Williams KS. *Gauss and Jacobi Sum*. Wiley: New York, 1998.
24. Sesia S, Toufik I, Baker M. *LTE-The UMTS Long Term Evolution: From Theory to Practice*. Wiley: Chichester, 2011.
25. Song MK, Bhargava VK. Performance analysis of cell search in W-CDMA systems over Rayleigh fading channels. *IEEE Transaction on Vehicular Technology* 2002; **51**(4): 749–759
26. Peebles PZ. *Probability, Random Variables, and Random Signal Principles*. McGraw-Hill: New York, 2001.
27. Hammarwall D, Bengtsson M, Ottersten B. Acquiring partial CSI for spatially selective transmission by instantaneous channel norm feedback. *IEEE Transaction on Signal Processing* 2008; **56**(3): 1188–1204
28. 3GPP TS 36.211. Physical channels and modulation. *Technical Report* (Release 13), 2016.
29. 3GPP TR 36.873. Study on 3D channel for LTE. *Technical Report* (Release 12), 2013.
30. Litva J, Lo TKY. *Digital Beamforming in Wireless Communications*. Artech House: Norwood, 1996.
31. Trees HLV. *Optimum Array Processing: Part IV of Detection, Estimation, and Modulation Theory*. Wiley: New York, 2002.

AUTHORS' BIOGRAPHIES

Rothna Pec received his B.S. and. M.S. degrees from the Institute of Technology of Cambodia, Chung-Ang University, Seoul, Korea, in 2011 and in 2013, respectively. He is currently pursuing his Ph.D. degree in electrical and electronics engineering at Chung-Ang University, Seoul, Korea. His research interests are in the area of digital signal processing and wireless communication systems.

Chang Hwan Park received his B.S., M.S, and Ph.D degrees in electrical and electronics engineering from Chung-Ang University, Seoul, Korea, in 2005, 2007, and 2011, respectively. In 2011, he joined LG Electronics Company, Seoul, Korea, as a deputy principle research engineer and has been involved in standardization activities of LTE in 3GPP and developing a Multi-MODEM chipset for HSPA+ and LTE-A. His research interests are in the area of mobile communication and digital signal processing, especially for MIMO-OFDM and 5G.

Yong Soo Cho received his B.S. degree in electronics engineering from Chung-Ang University, Seoul, Korea, the M.S. degree in electronics engineering from Yonsei University, Seoul, Korea, and his Ph.D degree in electrical and computer engineering from the University of Texas at Austin, in 1984, 1987, and 1991, respectively. During 1984, he was a Research Engineer at Goldstar Electrical Company, Osan, Korea. In 2001, he was a Visiting Research Fellow at Electronics and Telecommunications Research Institute (ETRI). In 1992, he joined Chung-Ang University, where he is currently Professor of School of Electrical and Electronic Engineering. His research interests are in the area of wireless communication, especially for MIMO-OFDM and 5G.

DOI: 10.1002/wcm